esteem3

Enabling Science through European Electron Microscopy

Report on the effects of radiolysis in liquid cells

Deliverable D6.3 – version 1

Estimated delivery date: 30th of June 2021

Actual delivery date: 23rd of June 2021

Lead beneficiary: JSI

Person responsible: Miran Čeh

Deliverable type: ☒ R ☐ DEM ☐ DEC ☐ OTHER ☐ ETHICS ☐ ORDP

Grant Agreement No:	823802
Funding Instrument:	Research and Innovation Actions (RIA)
Funded under:	H2020-INFRAIA-2018-1: Integrating Activities for Advanced Communities
Starting date:	01.01.2019
Duration:	48 months

Table of contents

Revision history log

Version number	Date of release	Author	Summary of changes
V0.1	18. 6. 2021	Bojan Ambrožič	Deliverable D6.3 – version 1
V0.2	21.06.2021	Miran Čeh	Deliverable D6.3 – version 2
V1	22.06.2021	Peter van Aken	Approval of deliverable

Sample preparation

The in-situ heating holder (trademark name P300) was produced by the manufacturer Protochips, Inc., Raleigh, NC.

The most important part of the holder is the titanium tip. The holder tip contains a chamber for the liquid and places for the inner and outer O-rings, which provide the vacuum seal. Through the holder, two intake and one outtake tubes are passing through and they re-emerge at the bottom of the liquid chamber. The inner diameters of intake and outtake tubes are 100 μm and 150 μm, respectively. This is to prevent pressure build-up inside the liquid cell. The intake and outtake tubes are made with polyether ether ketone (PEEK) tubing connected with specialized syringe pumps, which provide the push flow of liquid through the entire system. The holder is designed for the maximum liquid flow of 83 nL/s.

The liquid inside the holder is kept in between two silicon chips (usually called the large and small chips) with a 40-nm-thick Si_3N_4 windows for observing the liquid inside the TEM (Ahmad et al. 2017). The large chips (size 2 x 4.5 mm) contain electrodes and tungsten heating coils for heating the liquid (Williamson et al. 2003). The small chips (size of 2.0 x 4.5 mm) contain rectangular-shaped gold spacers (Nielsen et al. 2014). The spacers define the thickness of the liquid and the type of experiment (static or dynamic experiments). There are 50 nm, 150 nm, 500 nm, 2000 nm, and 5000 nm thick spacers available. Consequently, the spacers also define the volume of liquid inside the liquid cell. The volumes for the mentioned spacers are: 0.2 nL, 0.6 nL, 2 nL, 8 nL and 20 nL, respectively. Reducing the liquid thickness improved the TEM resolution; however, the radiolysis effects in the smaller volume of liquid are higher.

The temperature of the liquid in the liquid cell was controlled indirectly by applying an electric current through the tungsten coils located on the large chip. The electrical current was applied with a Keithley controller via the Protochips Poseidon V2.0.4 software with a calibration curve that was also provided by the manufacturer. With this system, a temperature range between 20 °C and 100 °C could be achieved. The heating rate could be set from 0.1 °C/min to a maximum of 10 °C/s. The temperature increase of the liquid as a result of the electron beam irradiation was not taken into consideration, as it was shown in several studies that for the given experimental beam currents the temperature can rise only by a few °C (Egerton, Li, and Malac 2004; J M Grogan et al. 2014). After heating, electronic cooling was not possible. The samples cooled naturally with heat dissipation. The cooling rates dropped asymptotically, and the average cooling rate at the temperature of 60 °C was ≈ 0.6 °C/s.

Experiments inside the in-situ heating holder can be performed in either the "static" or "dynamic" mode. The static mode refers to pouring a liquid drop between the chips and sealing all the tubing with specialized plastic plugs. For "static" mode experiments, special chips with spacers that encircle the entire chip were required (Nielsen et al. 2014). Dynamic modes refer to the flow of liquid through the holder tip. It is possible to flow one type of liquid through the first intake pipe and different types of liquid through the second intake pipe, and consequently observe how the two liquids are mixed and observed inside the liquid cell. One of the two intake pipes could also be vacuum-sealed, which allows observation of the flow of only one single type of liquid through the holder. All the heating experiments in this thesis were in static mode.

LCTEM Experimental Procedures

Here, the full experimental procedure for the LCTEM experiments is shown. One of the aims of our experiments was to observe homogenous nucleation. For this process to occur, all possible nucleation agents (e.g. dust, contaminants, etc.) must be removed. Therefore, the tools and the sample preparation room were as clean and dust-free as it was possible. A special laboratory for LCTEM sample preparation was established at the Department for Nanostructured Materials at the JSI. The outlined procedure took around half to a full day to complete, not including the preparation of the sample. The same chips could be used in several different experiments. But due to the above-mentioned risk of contamination, this was strictly avoided. Steps 1-5 were similar in the case of both holders (in situ heating and in situ electrochemistry). However, steps 6 and 8 were different for each holder.

Step 1: Preparation of the chips

The procedure started with the preparation of the experimental solution used in the LCTEM experiments. SiN chips were shipped protected with a protective photoresist, which was removed before the use of the chips. We removed the photoresist by rinsing the chips in acetone and methanol for 1 minute. After the rinsing, the chips were air-dried. Careful measures were taken, so that during these procedures the electrodes or W coils were not scratched with tweezers. Initially, the chips are hydrophobic. For that reason, they were plasma cleaned for achieving good wetting of the sample liquid.

Step 2: Assembly of the holder

After the plasma cleaning of the chips, the delicate process of holder assembly took place. The first part of the assembly was placing the small chip on top of both O-rings inside of the in-situ heating holder. On the small chip sample, a drop of solution was pipetted with a precise pipet. The volume of the pipetted solution was always several orders of magnitude larger than the available space between the chips. Therefore, the solution was squeezed out during the assembly of the holder. The chips were covered with the titanium lid, which in correlation with the O-rings and brass screws provided the vacuum seal. The lid was screwed into place with three small brass screws. Even the slightest mistake in the described holder assembly procedure resulted in the total failure of the experiment. Especially delicate were the thin SiN windows. An optical microscope was used to check if the window was intact.

Step 3: Leak check

After the holder was assembled it was inserted for 10 min into the vacuum leak check to check for possible leakage and to simulate the high-vacuum environment of a TEM. At the same time, it also acted as a drying agent to evaporate any remaining liquid and moisture that escaped between the O-rings. After that, the holder was removed from the leak check and inserted into the TEM.

Step 4: Insertion in the TEM

Once inside the TEM, the holder was connected to the tubing, syringe pumps, and (in case of in-situ heating experiments) to the Keithley controller (in-situ heating holder) /Gamry potentiostat (in-situ electrochemistry holder) and laptop computer. After that, the system was ready for in-situ liquid-cell experiments.

Step 5: TEM alignment

An important, however, frequently neglected, step related to a TEM is the microscope alignment. Usually, when performing conventional TEM analysis, the microscope is aligned and calibrated after the sample is already inserted into the microscope. However, in the case of LCTEM experiments, there were severe difficulties with this procedure due to the shifting liquid and radiolysis effects. Therefore, most calibration steps were performed before the insertion of the in-situ holder.

Step 6: LCTEM experiments

After that, the LCTEM holder containing the sample was inserted into the TEM, and the in-situ experiments were performed (Figure). In the case of the in situ heating experiments, the sample was usually investigated, i.e., observed by using the electron beam during the whole length of the experiment, utilizing video capturing. That allowed further analysis of the obtained videos, which provided important data for the interpretation of the videos.
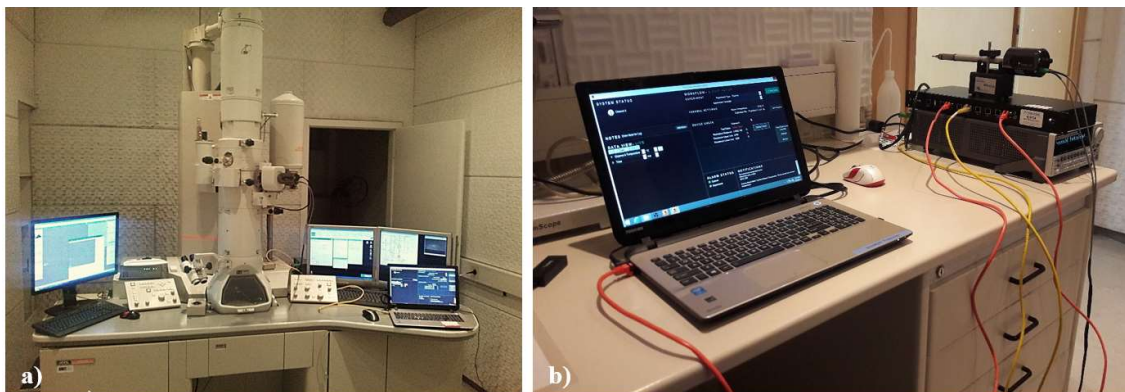
Figure 1: Fully assembled LCTEM set up (a) is controlled by a laptop computer connected to the Keithly controller (b).

Kinetic Radiolysis Model

This section presents an overview of the calculation for the kinetic radical-induced redox model. The details of the chemical kinetics, the reaction-rate constants, the primary yields, and the evaluation of various model parameters, which are experimentally difficult to assess, are included.

The temperature-/dose rate-dependent kinetic water-radiolysis model consists of reactions between the Au and the radiolytic species, being valid in the temperature range 20–100 °C for acidic and neutral initial solutions. For clarity, the calculated diagrams that are compared with the LCTEM are shown in the same temperature range 20–60 °C, matching the experimental conditions. The model includes the following species: e_{aq}^-, $H^\bullet$, $OH^\bullet$, H_2, H_2O_2, $HO_2^\bullet$, $HO_2^{-,}$ H^+, O_2, $O_2^{\bullet-}$, and OH^-. The reaction-rate coefficients were taken from the literature (Elliot, A.J. Bartels, D.M. 2009) and rewritten in the form of the Arrhenius relation. The primary yields, i.e., the G-values for the water radiolysis for the temperature range 20–100 °C were linearly interpolated from the tabulated G-values at 20 °C and 100 °C, (Elliot, A.J. Bartels, D.M. 2009) respectively.

The kinetic model was further corrected to take into account the presence of the gaseous phase. A common phenomenon observed during LCTEM is the formation of gas bubbles, (Shin et al. 2015; Zhu et al. 2013; Joseph M Grogan et al. 2014; Woehl et al. 2013) implying that the solubility of the formed gases in the liquid is exceeded during LCTEM. This is mainly due to the formation of molecular hydrogen and oxygen during the radiolysis. Figure shows the pressure due to the dissolved H_2 and O_2 in a temperature-/dose-rate-dependent diagram for the equilibrium state. The temperature-dependent solubility values for H_2 and O_2 were obtained from the National Institute of Standards and Technology (NIST) (Young 1981b; Battino 1981a) and the initial pH was 2.8, assuming that all the liquid in the cell was evenly irradiated by the electron beam (Figure). The acidic initial pH was desirable, since it is the least prone to radiolysis effects (Schneider, Norton, Mendel, Grogan, Ross, et al. 2014). The initial pH of 2.8 was chosen, because the radiolytic species do not have a significant influence on the pH of the acidic solutions (Schneider, Norton, Mendel, Grogan, Ross, et al. 2014). The desired pH value was achieved by preparing 1.5 mM $HAuCl_4$ solution. The inset shows a schematic of the LCTEM system, including the gaseous phase, where the thin liquid film (~ 50 nm (Joseph M Grogan et al. 2014)) enables O_2 and H_2 transfer between the liquid and the gas in a period of µs.
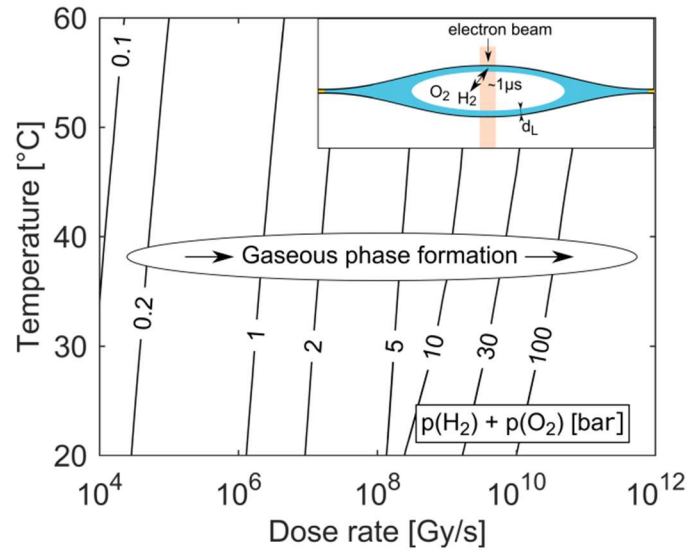
Figure 2: Pressure due to dissolved H_2 and O_2 in the equilibrium state for the water-radiolysis simulation. The initial pH is set to 2.8, with no initially dissolved O_2 or H_2. The inset shows a schematic representation of the LCTEM system with the gaseous phase. The liquid layer is very thin ($d_L \sim 50$ nm), allowing O_2 and H_2 transfer between the liquid and the gas in a period of μs.

As the partial pressure of water only changes from 0.023 bar at 20 °C to 0.199 bar at 60 °C, we can assume that the influence of the water's partial pressure on the overall pressure in the gas phase is negligible. This suggests that the pressure increase in the closed-cell is predominately controlled by the electron dose rate, which provokes the formation of H_2 and O_2 due to water radiolysis. It was experimentally confirmed that a liquid cell with similar dimensions can withstand a pressure of 4 bar (Xin et al. 2013). In practice, a large pressure increase is only expected at high dose rates, since only a small portion of the solution is irradiated by the electron beam. The pressure can also be partially compensated by the bowing of the SiN window(Ngo and Yang 2015).

Figure shows the equilibrium concentrations of the radiolysis products under typical LCTEM conditions for the Au system: a dose rate of 10^7 Gy/s and an initial pH of 2.8 in the temperature range 20–60 °C. The equilibrium concentrations of the radiolysis species were calculated at two limiting pressures in the liquid cells, i.e., at 1 bar and 5 bar (Figure). The pressure-dependent differences in the equilibrium concentration of the radiolysis species are visible (Figure). The concentrations of $H^\bullet$, $e^-_{aq,}$ and $OH^\bullet$ decrease by 20–50%, when the pressure increases from 1 bar to 5 bar. Moreover, these graphs also indicate that the temperature affects the equilibrium concentrations of the radiolysis species (notice that the concentrations in Figure are on a logarithmic scale). Importantly, all of them exhibit the same decreasing trend with the temperature increase.
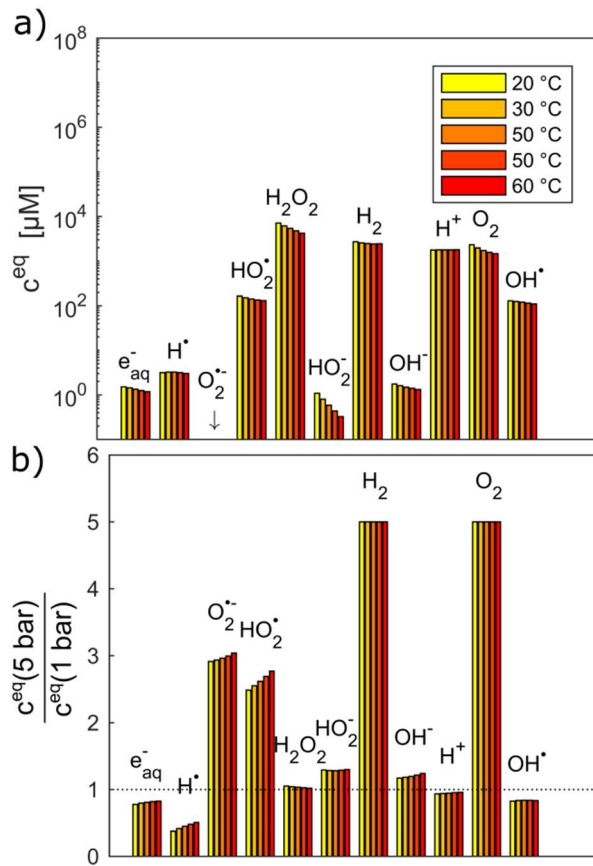
Figure 3: Equilibrium concentrations of radiolysis species in water at a dose rate of 10^7 Gy/s, pH_{init} = 2.8 and the temperature range 20–60 °C calculated at a) 1 bar and b) relative difference of equilibrium concentrations between 1 and 5 bar.

To estimate the influence of the radiolysis products on the precipitation/dissolution of Au the standard reduction potentials vs. SHE of the relevant half-cell reactions are listed in **Erreur ! Source du renvoi introuvable.**.

Table 1 : Standard electrode and Nernst electrode potentials vs. SHE of the involved half-cell reactions.

Half cell	E_0 [V]	E_{NERNST} [V]	Source E_0
$e^- + [AuCl_2]^- \rightleftharpoons Au^o + 2\ Cl^-$	1.15	0.97 ± 0.03	(Lingane 1962)
$e^- + H_2O \rightleftharpoons e^-_{aq}$	-2.79	-2.28 ± 0.36	(Buxton et al. 1988)
$e^- + H^+ \rightleftharpoons H^\bullet$	-2.23	-2.09 ± 0.15	(Buxton et al. 1988)
$O_2 + H^+ + e^- \rightleftharpoons HO_2^\bullet$	-0.04	-0.27 ± 0.12	(Schwarz 1981)
$2\ H_2O + 2\ e^- \rightleftharpoons H_2 + 2\ OH^-$	-0.83	-0.26 ± 0.42	(Bratsch 1989)
$2\ H^+ + 2\ e^- \rightleftharpoons H_2$	0.00	-0.09 ± 0.05	(Bratsch 1989)
$O_2 + e^- \rightleftharpoons O_2^{\bullet-}$	-0.33	0.05 ± 0.14	(Schwarz 1981)
$O_2 + 2\ H^+ + 2\ e^- \rightleftharpoons H_2O_2$	0.70	0.49 ± 0.12	(Bratsch 1989)
$O_2^- + H^+ + e^- \rightleftharpoons HO_2^-$	1.02	0.65 ± 0.16	(Schwarz 1981)
$O_2 + 2\ H_2O + 4\ e^- \rightleftharpoons 4\ OH^-$	0.40	0.78 ± 0.28	(Bratsch 1989)
$HO_2^\bullet + e^- \rightleftharpoons HO_2^-$	0.73	0.88 ± 0.24	(Schwarz 1981)
$O_2^{\bullet-} + 2\ H^+ + e^- \rightleftharpoons H_2O_2$	1.73	0.92 ± 0.28	(Schwarz 1981)
$O_2 + 2\ H^+ + 4\ e^- \rightleftharpoons 2\ H_2O$	1.27	0.98 ± 0.12	(Bratsch 1989)
$H_2O_2 + 2\ H^+ + e^- \rightleftharpoons 2\ H_2O$	1.76	1.05 ± 0.25	(Bratsch 1989)
$HO_2^\bullet + H^+ + e^- \rightleftharpoons H_2O_2$	1.46	1.18 ± 0.13	(Armstrong, D. A., Huie; R. E.; Lymar, S.;Koppenol, W. H.;Merényi, G.; Neta, P.; Ruscic, B.; Stanbury, D. M.; Steenken 2015)
$OH^\bullet + e^- \rightleftharpoons OH^-$	1.83	1.95 ± 0.12	(Schwarz 1981)

The reductive potentials vs. SHE using the Nernst equation for various in situ equilibrium conditions that are experimentally more relevant are additionally calculated. The average E_{NERNST} was calculated for the following conditions: $pH_{initial}$ 2.8, dose rates 10^6–10^{12} Gy/s, temperature 20–60 °C. From the reductive potentials of the half cells for Au and different radiolysis products, it is clear that the Au species can be reduced in the presence of e^-_{aq}, $H^\bullet$, H_2O_2, HO_2^-, H_2, $HO_2^\bullet$, $O_2^{\bullet-}$ and can be oxidized in the presence of $OH^\bullet$ radicals. The strongest reducing agents are e^-_{aq} (E_0 = -2.79 V_{SHE}, E_{NERNST} = -2.28 ± 0.36 V_{SHE}) and $H^\bullet$ (E_0 = -2.23 V_{SHE}, E_{NERNST} = -2.09 ± 0.15 V_{SHE}), which cause rapid metal precipitation (Ghosh Mazumdar, A. S. and Hart 1968), while $OH^\bullet$ (E_0 = 1.83 V_{SHE}, E_{NERNST} = 1.95 ± 0.12 V_{SHE}), as a strong oxidative agent, causes metal dissolution (Alloyeau et al. 2015). The reaction-rate coefficients between the radiolysis products and the Au species indicate that the $H^\bullet$, $OH^\bullet$ radicals, and e^-_{aq} have a much stronger effect on the gold species compared to the other solutes (Table).

Table 2: Reaction-rate constants of radiolysis products with gold species.

Au spec.	Radiolysis spec	k_{20} °C [M^{-1}s^{-1}]	E_A [kJ/mol]	$A_{calculated}$
Au$^+$	e^-_{aq}	8.0×10^9	12.98	1.64×10^{12}
	$H^\bullet$	8.0×10^9	15.09	3.91×10^{12}
	H_2O_2	0	0	0
	HO_2^-	1.89	25.8	7.46×10^4
	H_2	7.4×10^{-3}	94.1	4.28×10^{14}
	$HO_2^\bullet$	1.89	25.8	7.46×10^4
	$O_2^{\bullet-}$	1.89	25.8	7.46×10^4
Au^0	$OH^\bullet$	1.83×10^9	13.0	3.80×10^{11}

The primary aim of this study is to model and control the radical-induced redox chemistry in a LCTEM that is based on the precipitation/dissolution of Au NPs, which we used as a model system. Accordingly, we have simplified the model to a homogeneous system, which means the reduced Au species are introduced in the form of concentration and are all available for oxidation reactions. Additionally, it is assumed that all the Au ions are in the form of Au$^+$, as we want to observe only the transition between the Au^0 atoms and the Au$^+$ ions. The concentrations of the Au species are incorporated into the model like any other component, where the reaction-rate constants between the radiolysis products and the Au species were taken from Table 2. The corresponding rate of Au-species production is shown in the following equation

$$\frac{dc_{Au^+}}{dt} = -\frac{dc_{Au^0}}{dt} = \sum_i k_{i-Au^0} c_i c_{Au^0} - \sum_i k_{i-Au^+} c_i c_{Au^+},$$

where c_{Au^+} and c_{Au^0} represent the concentrations of gold ions and gold atoms, respectively. The reaction-rate constants for the reactions between the i compound with the gold species are indicated by k_{i-Au^0} and k_{i-Au^+}. Using this equation, we estimated that the steady-state, i.e., the equilibrium concentration of the gold species, is achieved after 10^{-3} s.

The resulting equilibrium ratio of *[Au^0]/[Au$^+$]* in our model can be taken as an indicator of the reductive/oxidative ratio between the ionic, i.e., dissolved, and the solid, i.e., precipitated, gold. The latter will form Au NPs in the liquid cell. These theoretically obtained values can be translated into the LCTEM experiment by assuming that the Au precipitation or dissolution is directly related to the equilibrium ratio *[Au^0]/*[Au$^+$], thus providing the same kind of information. For example, a *[Au^0]/[Au$^+$]* gradient increase indicates the gold's tendency for precipitation and growth, resulting in the formation of Au NPs. In contrast, a *[Au^0]/[Au$^+$]* gradient decrease signifies either the inability of Au to precipitate or the dissolution of the already-formed Au NPs (Figure 4). These are the phenomena that can be easily observed during the LCTEM.
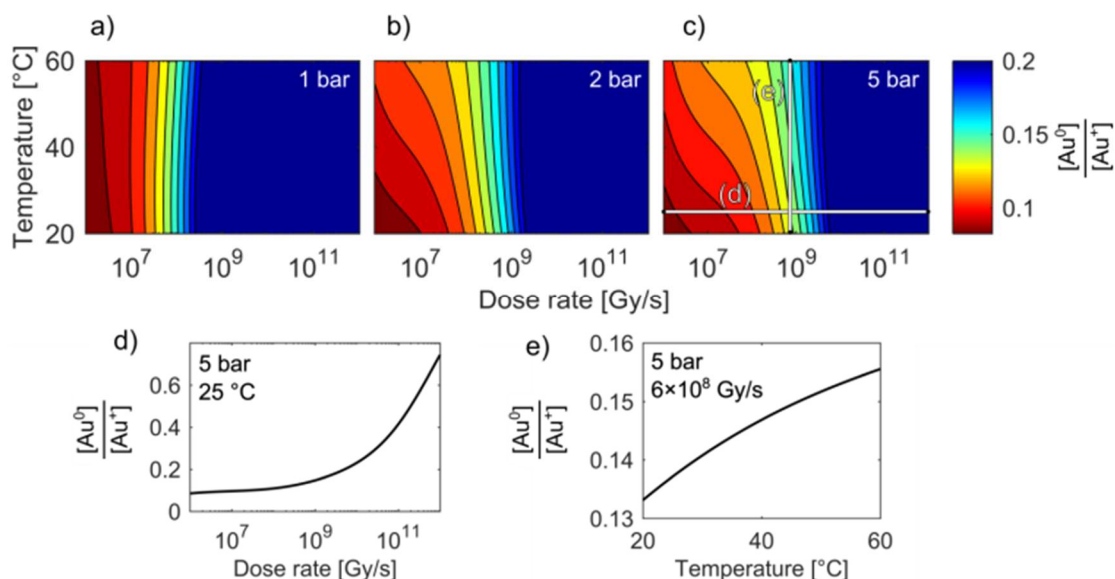
Figure 4: Temperature/Dose-rate Redox ratio (TDR) diagrams (a-c). Note that the stability regions for the equilibrium $[Au^o]/[Au^+]$ concentrations in the LCTEM are, in addition to dose-rate and temperature, also pressure dependent. Initial $[Au^+]$ = 1.5 mM, $pH_{initial}$ = 2.8. Figures d) and e) show sections of the Au redox ratio trends from diagram c).

Temperature/Dose-rate Redox ratio (TDR) diagrams, showing different redox *[Au^o]/[Au^+]* stability regions, are shown in Figure . The TDR diagrams are calculated for the dose-rate range 10^6–10^{12} Gy/s, temperature range 20–60 °C, and at the H_2+O_2 pressures 1 bar, 3 bar, and 5 bar, with the molar ratio in the gaseous phase H_2/O_2 = 2. The resulting equilibrium redox concentration ratio of *[Au^o]/[Au^+]* was obtained for an initial concentration of Au^+ species of 1.5 mM and a corresponding pH of 2.8. The calculated TDR diagrams are characterized with distinctive regions, where the conditions in the LCTEM tend towards a reducing environment that will promote the precipitation of Au NPs (blue). In contrast, the oxidative environment (dark red) will either prevent the formation of Au NPs or promote the Au NPs' dissolution. The following "rainbow" color code indicates the intermediate conditions between the oxidative and reductive extremes.

When the pressure in the cell is set to 1 bar, the temperature does not have any significant effect on the Au redox ratio (Figure). In that case, a change in the dose rate has a much larger impact on the Au redox ratio, when compared with a temperature change. This implies that the precipitation of gold is positively and monotonously correlated with an increase in the dose rate, as was previously reported by Schneider et al. (Schneider, Norton, Mendel, Grogan, Ross, et al. 2014).

However, our results indicate that even at intermediate dose rates the saturation concentration for the solubility of H_2 and O_2 in the aqueous solutions will be exceeded and the radiolysis model is better defined by considering the elevated-pressure regimes inside the LCTEM system. The resulting model at elevated pressure (5 bars) indicates that the effect of temperature on the Au redox ratio starts to become significant, which is most pronounced at low and intermediate dose rates that are typically used during LCTEM. The effect of the temperature on the redox conditions can be explained by the scavenging effect of the H_2 and O_2 species, i.e., H_2 is a strong $OH^\bullet$ scavenger, while O_2 is a strong scavenger of $H^\bullet$ and e^-_{aq}. Due to the presence of the gaseous phase, the concentrations of H_2 and O_2 are mainly dependent on the finite pressure and solubility limits. Moreover, with a temperature increase, the O_2 solubility will decrease at higher rates when compared to the H_2 solubility. As a result, a smaller amount of $H^\bullet$ and e^-_{aq} scavengers at higher temperatures pushes the system towards more reductive conditions, as is evident in Figure for pressures of 3–5 bars. The sensitivity analysis of the temperature-dependent part of the H_2 and O_2 solubility supports this explanation and is elaborated.

Model Verification by Low-Dose Experiments Using γ Radiation

Before the LCTEM, the model was validated with a quantitative comparison using literature reports (Pastina and Laverne 2001; Hayon 1963; Hochanadel 1952) of radiolysis products obtained by irradiating water with low-dose γ-radiation. Electron radiation is a low-LET (linear energy transfer) radiation and is similar to γ-radiation. Hill (Hill and Smith 1994) calculated the primary yields for different electron energies and observed constant yields above 10 keV. Temperature-dependent primary yields were obtained for water at neutral pH from Elliot and Bartels (Elliot, A.J. Bartels, D.M. 2009). The experiments were performed at different dose rates and solute concentrations. Figure shows different sets of experimental H_2O_2 concentration data obtained by irradiating water with low-dose γ-radiation under various experimental conditions as a function of time. It is worth mentioning that every data set is obtained from a different literature source (Pastina and Laverne 2001; Hayon 1963; Hochanadel 1952). Only the experimental data for concentration variations of H_2O_2, H_2, and O_2 are reported here. Individual experimental data points are represented by color-coded dots, while the corresponding color-coded solid lines are obtained from the kinetic radiolysis model developed in this study using the given low-dose γ-radiation experimental conditions. For example, Figure shows the concentration variations of H_2O_2 for different initial concentrations of H_2, while Figure shows H_2O_2 variations for different initial values of H_2O_2. Figure indicates the concentration changes of H_2O_2 when varying the initial concentration of both H_2 and O_2. Remarkably, although not at the same time, our model accurately predicts the abrupt drop of the H_2O_2 concentration for the case of initial H_2 and O_2 concentrations of 7.31×10^{-4} and 7.50×10^{-5} M, respectively (shown in the yellow-coded color). By comparing the result of our kinetic radiolysis model with the experimental data for low-dose γ radiation (Figure 5) (~1 Gy/s), (Pastina and Laverne 2001; Hochanadel 1952; Hayon 1963) it is evident that the proposed radiolysis model fits very well with the experimentally obtained data.
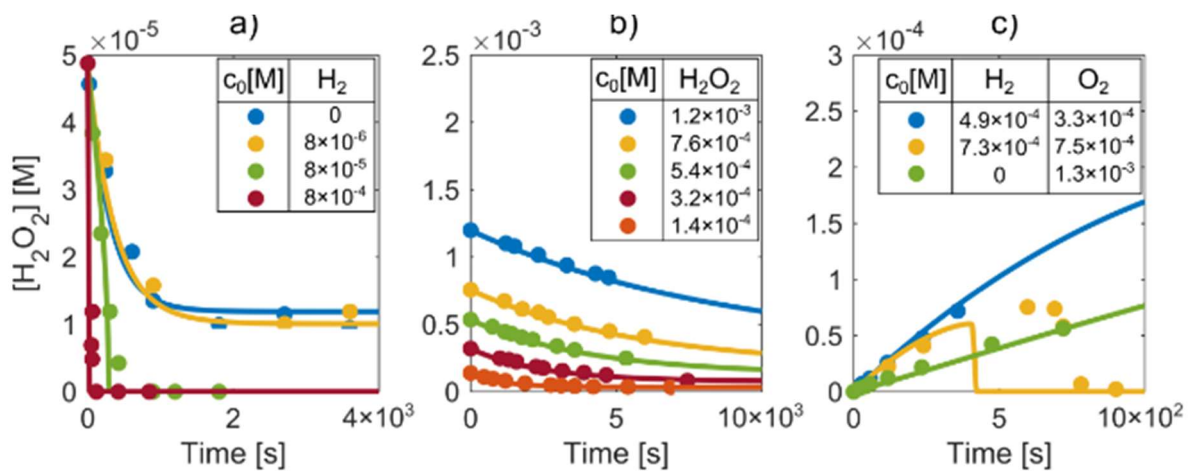

Figure 5: Determination of H_2O_2 concentrations during the irradiation of water with low-dose γ radiation for different initial a) H_2, b) H_2O_2, and c) H_2 and O_2 concentrations (marked by color-coded dots). The corresponding color-coded solid lines represent the prediction of our radiolysis model.

The conditions used for our model verification were collected from several sources (Pastina and Laverne 2001; Hayon 1963; Hochanadel 1952) for the bulk water radiolysis in solutions of H_2O_2, O_2, and H_2 by using γ rays as a source of radiation, which is similar to electron radiation low-LET (linear energy transfer). The experiments were performed at different dose rates and solute concentrations (Table).

Table 3: Detailed conditions of the radiolysis model's verification.

source	Line	Dose rate [Gy/s]	T [°C]	c_{init} [M]			
				pH_{init}	H_2O_2	O_2	H_2
Pastina, LaVerne 2001 (Pastina and Laverne 2001)	1	0.250	25	7	4.88×10^{-5}	0	0
	2	0.250	25	7	4.88×10^{-3}	0	8.00×10^{-6}
	3	0.250	25	7	4.88×10^{-5}	0	8.00×10^{-5}
	4	0.250	25	7	4.88×10^{-5}	0	8.00×10^{-4}
Hayon 1963(Hayon 1963)	1	0.205	25	7	1.20×10^{-3}	0	0
	2	0.205	25	7	7.57×10^{-4}	0	0
	3	0.205	25	7	5.35×10^{-4}	0	0
	4	0.205	25	7	3.20×10^{-4}	0	0
	4	0.205	25	7	1.39×10^{-4}	0	0
(Hochanadel 1952) Hochandel 1952 (Hochanadel 1952)	1	0.653	25	7	0	3.32×10^{-4}	4.90×10^{-4}
	2	0.653	25	7	0	7.50×10^{-5}	7.31×10^{-4}
	3	0.653	25	7	0	1.25×10^{-3}	0

General Model Description of Water Radiolysis:

The $O^{\bullet-}$, O_3, $HO_3^{\bullet}$, $O_3^{\bullet}$ species were not included in the model due to the lack of any corresponding kinetic data at higher temperatures. These species are predominantly formed in basic solutions. This is due to the deprotonation of the hydroxyl radical ($OH^{\bullet}$) into $O^{\bullet-}$ ($pK_a \approx 11$ (Elliot, A.J. Bartels, D.M. 2009)) and H_2O_2 into HO_2^- ($pK_a \approx 11$ (Elliot, A.J. Bartels, D.M. 2009)). The presence of the oxygen anion and the hydroperoxyl anion is responsible for the formation of the ozone anion and subsequently other ozonide species (Elliot, A.J. Bartels, D.M. 2009). To justify the model's simplification, we calculated the ratio between the sum of the equilibrium concentrations of $O^{\bullet-}$, O_3, $HO_3^{\bullet}$, O_3^- and the equilibrium concentrations of the $OH^{\bullet}$ radical, using the correlations for equilibrium concentrations in a homogenous solution (Schneider, Norton, Mendel, Grogan, Ross, et al. 2014) at an initial pH 7 and 20 °C. At 10^{10} Gy/s (upper limit of the power-law model), the ratio is 0.012; therefore, there are approximately 80-times more $OH^{\bullet}$ radicals than other strong oxidizing species (Figure 5). Due to the lower deprotonation rate at lower pH, the ratio of these concentrations is even lower, leaving the $OH^{\bullet}$ radical as the main strong oxidizing agent.
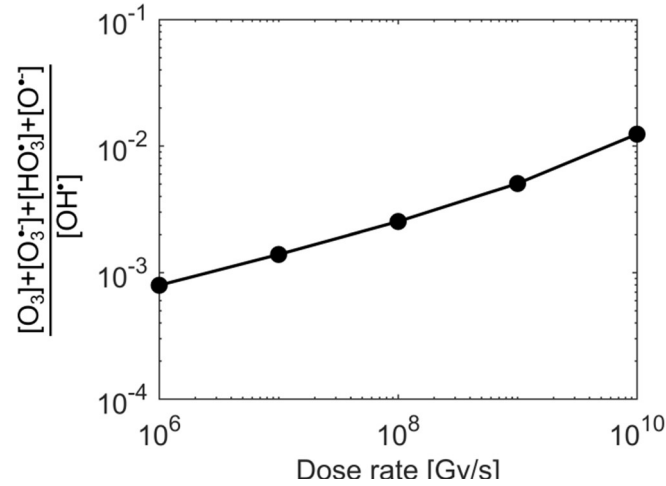
Figure 5: Validity of the simplification of the reaction scheme: the dose-rate dependence of the ratio of the equilibrium concentration between $O^{\bullet-}$, O_3, HO_3, O_3^- and $OH^{\bullet}$ radicals at an initial pH = 7 and 20 °C.

According to the Arrhenius plots in Elliot et al. (Elliot, A.J. Bartels, D.M. 2009), all the reaction-rate constants linearly follow the relation $\ln(k) \propto T^{-1}$ below 100 °C. Therefore, the temperature dependence is written in the form of activation energies and pre-exponential factors. The processes in the irradiated matter can be described with a mass-balance equation with the reaction parts and the radiolysis primary yields:

$$\frac{dc_i}{dt} = -\sum_j k_{ij}\, c_i c_j + \sum_{j,k \neq i} k_{jk}\, c_j c_k + R_i,$$

where c_i represents the concentrations of the individual species, k_{ij} represents the reaction-rate constant and R_i represent the radiolytic yield. The first part of the right-hand side of the equation describes the consumption rate of the i compound, while the second part describes the formation of the i compound. The radiolytic yield R_i is the formation or consumption rate of the j compound by radiolysis.

$$R_i = \frac{\rho \psi G_i}{F} \left[\frac{M}{s}\right]$$

In the above equation, ρ represents the solvent density, F is the Faraday constant, ψ is the dose rate of the radiation and G_i is a G value, which represents the primary yield of the i compound in the first 1 µs from the start of the radiation. This value is given as the number of molecules created or destroyed per 100 eV of energy deposited. The G values depend on the type of radiation, the media exposed to the radiation, and the temperature. They are given in Table 4. The temperature dependence of the G values is calculated using linear interpolation.

The dose rate ψ is calculated from the following equation:

$$\psi = \frac{S\, 10^5 I_b}{\pi a^2} \left[\frac{Gy}{s}\right]$$

where S [MeV cm²/g electron] is the density-normalized, stopping power in the medium, I_b is the beam current and a is the beam radius.

14

Table 4: Reaction-rate constants for the temperature range between 20 °C and 100 °C (Elliot, A.J. Bartels, D.M. 2009).

Reagents	Products	A [*]	E_A [kJ mol^{-1} K^{-1}]
$H^+ + OH^-$	H_2O_2	1.88×10^{13}	12.62
H_2O	$H^+ + OH^-$	1.70×10^6	62.37
H_2O_2	$H^+ + HO_2^-$	4.12×10^6	43.77
$H^+ + HO_2^-$	H_2O_2	5.59×10^{12}	11.73
$H_2O_2 + OH^-$	$HO_2^- + H_2O$	3.66×10^{12}	13.98
$HO_2^- + H_2O$	$H_2O_2 + OH^-$	4.54×10^{11}	31.74
$e^-_{aq} + H_2O$	$H^\bullet + OH^-$	5.58×10^6	31.73
$H^\bullet + OH^-$	$e^-_{aq} + H_2O$	8.52×10^{13}	37.36
$H^\bullet$	$H^+ + e^-_{aq}$	2.84×10^{12}	66.66
$H^+ + e^-_{aq}$	$H^\bullet$	1.98×10^{12}	11.17
$HO_2^\bullet$	$O_2^{\bullet-} + H^+$	2.63×10^8	14.58
$O_2^{\bullet-} + H^+$	$HO_2^\bullet$	5.59×10^{12}	11.73
$HO_2^\bullet + OH^-$	$O_2^{\bullet-} + H_2O$	7.13×10^9	60.93
$O_2^{\bullet-} + H_2O$	$HO_2^\bullet + OH^-$	3.66×10^{12}	13.98
$e^-_{aq} + OH^\bullet$	OH^-	2.64×10^{12}	10.65
$e^-_{aq} + H_2O_2$	$OH^\bullet + OH^-$	7.75×10^{12}	15.72
$e^-_{aq} + H_2O + O_2^{\bullet-}$	$HO_2^- + OH^-$	4.43×10^{10}	12.98
$e^-_{aq} + HO_2^\bullet$	HO_2^-	2.45×10^{12}	12.98
$e^-_{aq} + O_2$	$O_2^{\bullet-}$	2.53×10^{12}	11.66
$e^-_{aq} + e^-_{aq} + H_2O + H_2O$	$H_2 + OH^- + OH^-$	1.01×10^{10}	20.74
$e^-_{aq} + H^\bullet + H_2O$	$H_2 + OH^-$	2.06×10^{11}	14.93
$H^\bullet + H_2O$	$H_2 + OH^\bullet$	7.39×10^{12}	98.24
$H^\bullet + H^\bullet$	H_2	2.69×10^{12}	15.51
$H^\bullet + OH^\bullet$	H_2O	4.19×10^{11}	9.03
$H^\bullet + H_2O_2$	$OH^\bullet + H_2O$	1.76×10^{11}	21.01
$H^\bullet + O_2$	$HO_2^\bullet$	9.01×10^{11}	10.52
$H^\bullet + HO_2^\bullet$	H_2O_2	5.05×10^{12}	15.09
$H^\bullet + O_2^{\bullet-}$	HO_2^-	5.05×10^{12}	15.09
$OH^\bullet + OH^\bullet$	H_2O_2	9.78×10^{10}	7.48
$OH^\bullet + HO_2^\bullet$	$O_2 + H_2O$	1.31×10^{11}	6.68
$OH^\bullet + O_2^{\bullet-}$	$OH^- + O_2$	8.75×10^{11}	10.84

$H_2 + OH^\bullet$	$H^\bullet + H_2O$	6.55×10^{10}	18.45
$OH^\bullet + H_2O_2$	$HO_2^\bullet + H_2O$	7.72×10^9	13.82
$OH^\bullet + HO_2^-$	$HO_2^\bullet + OH^-$	1.00×10^{12}	11.92
$HO_2^\bullet + O_2^{\bullet-}$	$HO_2^- + O_2$	2.62×10^9	8.09
$HO_2^\bullet + HO_2^\bullet$	$O_2 + H_2O_2$	2.77×10^9	20.07

*for the reactions with one molecule the unit is $[s^{-1}]$, for two molecules $[M^{-1}s^{-1}]$, for three molecules $[M^{-2}s^{-1}]$ and for four molecules $[M^{-3}s^{-1}]$. We used 55.56 M as the molar concentration of water.

Table 5: Primary yields, G values, for the temperature range between 20 C and 100 C.

Species	G_{i-20} °C $[N_i/100eV]$	G_{i-100} °C $[N_i/100eV]$	Source
e^-_{aq}	2.73	3.10	(Elliot, A.J. Bartels, D.M. 2009)
H^+	3.19	3.61	[a]
OH^-	0.46	0.51	[a]
H_2O_2	0.72	0.59	(Elliot, A.J. Bartels, D.M. 2009)
$H^\bullet$	0.60	0.71	(Elliot, A.J. Bartels, D.M. 2009)
$OH^\bullet$	2.75	3.57	(Elliot, A.J. Bartels, D.M. 2009)
H_2	0.43	0.47	(Elliot, A.J. Bartels, D.M. 2009)
H_2O	-4.65	-5.26	[b]

[a] H^+ primary yield is calculated using the ratio between $G(H^\bullet)$ and $G(e^-_{aq})$ obtained from experimental measurements (Green et al. 1990; Anderson, Vojnovic, and Michael 1985) that are summed in the work of Hill and Smith (Hill and Smith 1994). Using this ratio the charge-balance yield $G(OH^-)$ to 0.46 at 25 °C and 0.51 at 100 °C, which is a similar value to $G(OH^-) = 0.50$ for low LET radiation. (Pastina and Laverne 2001)
[b] Mass-balance calculation.

The Interaction Between the Radiolysis Products and the Gold Species in the LCTEM System:

Influence of chloride ions: chloride is an $OH^\bullet$ scavenger. The main reaction product due to the presence of chloride is $ClOH^{\bullet,-}$(Atinault et al. 2008), which is also a very strong oxidizer ($E_0(ClOH^\bullet/(Cl^-+OH^-))$) = 1.91 V_{SHE} (Armstrong, D. A., Huie; R. E.; Lymar, S.; Koppenol, W. H.; Merényi, G.; Neta, P.; Ruscic, B.; Stanbury, D. M.; Steenken 2015)) and can also oxidize Au particles. Due to the large difference in the standard electrochemical potentials between $ClOH^{\bullet-}$ and Au^0, it is assumed that the rate of Au oxidation with $OH^\bullet$ and $ClOH^{\bullet-}$ is similar, which is approximated to a negligible influence on the trends of the Au oxidation state. However, for an accurate assessment of the chloride influence, all the significant reactions with the chloride species should be added.
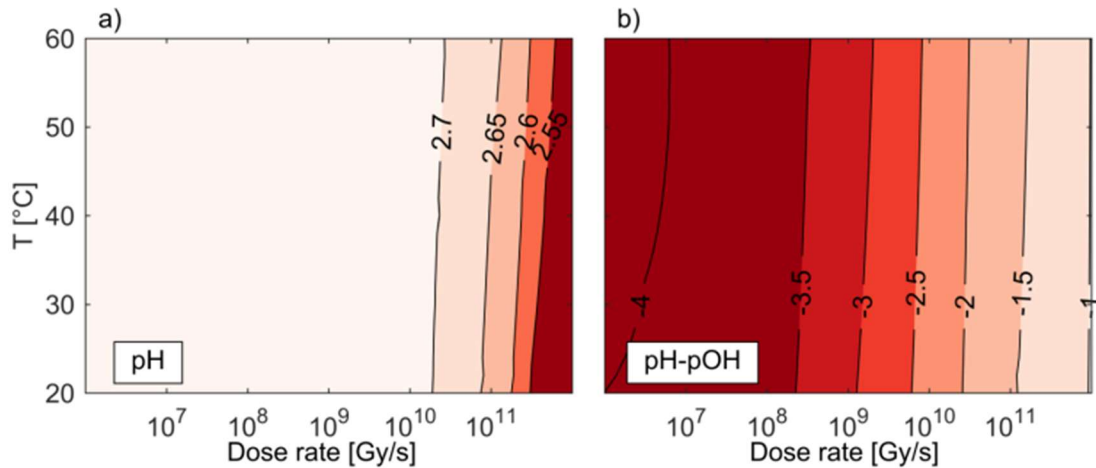
Figure 6 a) Equilibrium pH of the solution containing Au species. b) Equilibrium difference between pH and pOH. Initial pH = 2.8, maximum pressure 1 bar.

Calculation of pH and pOH (Table): The Au ions can form hydroxide species and other aureate species at higher values of pH (>7) and at high redox potentials (R Winston Revie; Herbert Henry Uhlig 2011). To evaluate the most stable gold species for the set experimental conditions, the values of the pH and pH-pOH were calculated. The graph indicates that the pH is stable at the initial pH value of 2.8 for the broad range of dose rates from 10^6 up to 10^{10} Gy/s. Above the indicated dose rate the pH value decreases from 2.7 to 2.55, when the dose rate is increased from 10^{10} to 10^{12} Gy/s, respectively. Relative to the dose rate, it was concluded that the pH variations are not significantly influenced by a change of the temperature in the LCTEM. However, to determine the chemical state of the gold species the OH^- concentration is also important. The difference pH-pOH is equal to $\log_{10}([OH^-]/[H^+])$ and ranges between -4 and -1, mainly influenced by the changes in the dose rates. Due to the relatively low pH value (2.7-2.6) and the pH-pOH value between -4 and -1 (more acidic solution) at all dose rates and temperatures, this study confirms that the dissolved Au species are in the form $[AuCl_2]^-$.

Table 6: Reaction-rate constants of the radiolysis products with gold species.

Au spec.	Radiolysis spec.	$k_{20\,°C}$ [$M^{-1}s^{-1}$]	Reference	E_A [kJ/mol]	Reference	A calculated
Au$^+$	e$^-_{aq}$	8.0×10^9	(Ghosh Mazumdar, A. S. and Hart 1968)	12.98[b]		1.64×10^{12}
	H$^\bullet$	$8.0 \times 10^{9\ a}$	(Ghosh Mazumdar, A. S. and Hart 1968)	15.09[c]		3.91×10^{12}
	H$_2$O$_2$	0 [j]	(Pacławski, K. and Fitzner 2006)	/	(Pacławski, K. and Fitzner 2006)	0
	HO$_2^-$	1.89[d]	(Pacławski, K. and Fitzner 2006)	25.8 [d,e]	(Pacławski, K. and Fitzner 2006)	7.46×10^4
	H$_2$	$7.4 \times 10^{-3\ d,\ f}$	(Ershov et al. 2016)	94.1[d,g]	(Wang et al. 2011)	4.28×10^{14}

	HO$_2^{\bullet}$	1.89 [d,h]		25.8 [d,h]		7.46 × 10^4
	O$_2^{\bullet-}$	1.89 [d,h]		25.8 [d,h]		7.46 × 10^4
Au^o	OH$^{\bullet}$	1.83 × 10^9 [i]		13.0 [i]		3.80 × 10^{11}

[a] Assumed the same k$_{20\,°C}$, as for the reaction between e$^-_{aq}$ and Au$^+$, because the reaction rate constants of Au^{+3}+H$^{\bullet}$/ e$^-_{aq}$ →Au^{+2}+H$^+$/H$_2$O are similar ((5.7 +/- 1.5) × 10^9 M^{-1}s^{-1} (Ghosh Mazumdar, A. S. and Hart 1968)).

[b] E_A assumed the same as for the reaction e$^-_{aq}$ +O$_2^{\bullet-}$(+ H$_2$O)→HO$_2^-$+OH$^-$, because both reactions are diffusion-controlled and O$_2^{\bullet-}$ as the [AuCl$_2$] $^-$ negatively charged.

[c] E_A assumed the same as for the reaction H$^{\bullet}$ + O$_2^{\bullet-}$→ HO$_2^-$, because both reactions are diffusion-controlled and O$_2^{\bullet-}$ is as the [AuCl$_2$]$^-$ negatively charged.

[d] Rate for the presence of a gold catalyst, as given in the literature.

[e] E_A from the overall observed constant is used (apparent activation energy). (Pacławski, K. and Fitzner 2006)

[f] Rate expression $k[Au^o][H_2]$, at pH = 7 (Ershov et al. 2016).

[g] E_A assumed for the H$_2$ dissociation on Au (211) (Wang et al. 2011), since it is the dissociation step.

[h] Assumed the same rate and activation energy as for the reaction HO$_2^-$+Au$^+$→HO$_2^{\bullet}$+Au^o. HO$_2^{\bullet}$ and O$_2^{\bullet-}$ are thermodynamically much stronger reducing agents (E_{NERNST} = -0.27 and 0.05 respectively) than HO$_2^-$ (E_{NERNST} = 0.65 However, in the density functional theory (DFT) study on Au (111) (Yang et al. 2017) they show, that the reaction H$_2$O$_2$*→HO$_2$*+H* has a lower activation energy (E_A = 113 kJ/mol, ΔE = 106 kJ/mol) than the reaction HO$_2$*→ O$_2$*+H* (E_a = 141 kJ/mol, ΔE = 85 kJ/mol). Also, it is found that at higher pH (10-13) the reduction of HAuCl$_4$ with H$_2$O$_2$ is more significant and much faster than at neutral pH (7–8)(Pacławski, K. and Fitzner 2006). This can be due to a larger amount of HO$_2^-$ and O$_2^{\bullet}$. The electron-transfer reactions are generally fast, and it is expected that O$_2^{\bullet}$ will reduce the Au species with a rate similar to H$^{\bullet}$ or e$^-_{aq}$. However, in the case of low pH, O$_2^{\bullet}$ is protonated to HO$_2^{\bullet}$, which needs to be broken on the Au surface to form O$_2$ and H*, and this is a much slower process, as seen from DFT calculations(Yang et al. 2017). Because of the lack of experimental data on the kinetics of HO$_2^{\bullet}$ and O$_2^{\bullet-}$ with Au$^+$, we assume the same rate as for the case of the reaction of HO$_2^-$ with Au$^+$. However, for the experiments at high pH, where the amounts of HO$_2^-$ and O$_2^{\bullet}$ are significant, corrected reaction rates should be used.

[i] Assumed the same rate coefficient as for the reaction of Au$^+$+OH$^{\bullet}$→Au^{+2} +OH$^-$. The rates of dissolution of Au^o with a strong oxidizing or complexing agent without stirring are usually diffusion controlled (Habahchi 1967). Because of zero stirring, the reaction is diffusion controlled. For the case of the dissolution of Au in a cyanide solution, the activation energies are 12–21 kJ/mol (Habahchi 1967). The temperature dependence of the diffusivity constant for water self-diffusion, which is similar to the OH$^{\bullet}$ diffusion constant, is used to calculate the activation energy (Elliot, A.J. Bartels, D.M. 2009).

[j] The value is 0, because the mechanism of Au-ion reduction proceeds through HO$_2^-$ (Pacławski, K. and Fitzner 2006). In the kinetic model, we have already included the reversible reaction between H$_2$O$_2$ and HO$_2^-$, and therefore the contribution to the reduction of the H$_2$O$_2$ is 0.

Explanation of Redox Trends Due to Temperature Change:

The influence of the temperature on $[Au^o]/[Au^+]$ increases with increasing pressure which points to the influence of the H$_2$ and O$_2$ solubility in the liquid phase. The temperature dependence of the O$_2$ solubility is significantly higher when compared with the solubility of H$_2$ in water (Table).

Table 7: Solubility of the H$_2$ and O$_2$ gases in water.

T	$\frac{1}{K_H}\Big|_{O_2}\left[\frac{mol}{L\,bar}\right]$	$\frac{1}{K_H}\Big|_{H_2}\left[\frac{mol}{L\,bar}\right]$

20 °C	1.40×10⁻³	8.08 ×10⁻⁴
60 °C	0.88×10⁻³ (decreased by 37% relative to 20 °C)	7.28 ×10⁻⁴ (decreased by 9.9% relative to 20 °C)

To prove the impact of the solubility's temperature dependence, we performed a sensitivity analysis for the temperature-dependent part of the solubility relation (of both gases at the same time). We calculated the Au redox ratios for the different *factor* values: 0.5, 1, and 2:

$$H_i(T(K)) = \exp\left(-A + \frac{B}{factor(T - 293.15\,K) + 293.15\,K}\right.$$

$$\left. + C\log_{10}((factor(T - 293.15\,K) + 293.15\,K)/100)\right) \frac{55.5\frac{mol}{L}}{1\,bar} \qquad (4.5)$$

Table 8: Parameters of the temperature-dependent Henry constant (Young 1981a; Battino 1981b).

Coef.	H₂	O₂
A	48.1611	66.7354
B	5528.45	8747.55
C	16.8893	24.4526

From Figure , we can see that the temperature dependence of the solubility influences the Au redox ratio. When we increase the temperature dependence of the gases' solubility (factor = 2) the redox ratio increases faster with temperature, and when we decrease the temperature dependence of the gases solubility (factor = 0.5), the redox ratio increases more slowly. The concentration of O_2 in the liquid phase decreases much faster than the concentration of H_2. Because H_2 is a strong OH• radical scavenger ($k_{20\,°C} = 3.4\times10^7\ M^{-1}s^{-1}$) and O_2 is a strong scavenger of H• and e^-_{aq} ($k_{20\,°C} = 1.2\times10^{10}, 2.1\times10^{10}\ M^{-1}s^{-1}$, respectively), the ratio $\frac{[H^•]+[e^-_{aq}]}{[OH^•]}$ (consequently Au redox ratio), depends on the concentrations of O_2 and H_2.
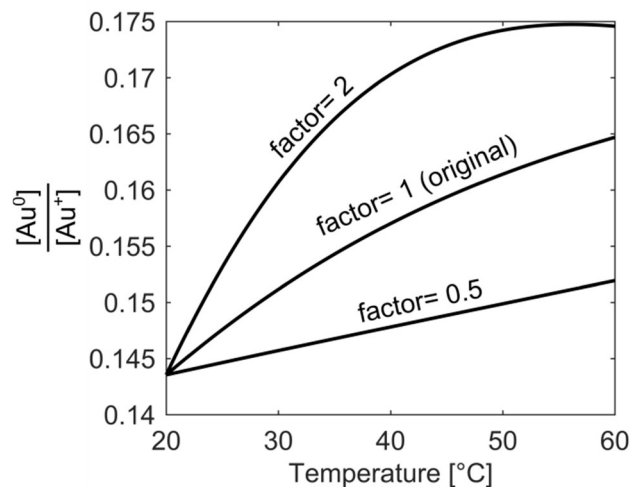

Figure 7: Temperature dependence of the Au redox ratio at different sensitivity factors of the H₂ and O₂ solubilities. Dose rate 10^9 Gy/s, total concentration of gold species is 1.5 mM with an initial pH 2.8, and pressure 5 bar.

19

LCTEM Synthesis of Gold Nanoparticles

Figure shows a time sequence of the precipitation and dissolution dynamics of Au NPs at a constant dose rate of 10^9 Gy/s and a temperature of 20 °C. A region, where representative Au NPs exhibit precipitation, growth, and dissolution on a time scale of 5 s, which is marked by an arrow or a dashed-line circle. At time 0 s, the Au NPs are not yet formed, it appears at 1.8 s., and remains stable for a period of approximately 3 s, followed by complete dissolution at 5.1 s.
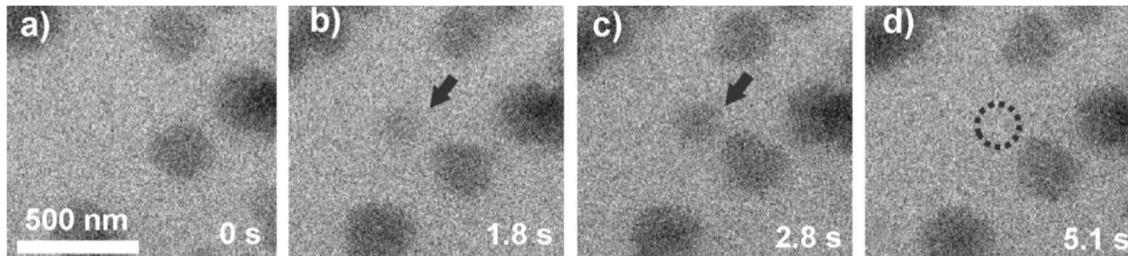
Figure 8: TEM micrographs indicating the precipitation and dissolution of Au NPs at a constant dose rate of 10^9 Gy/s and a temperature of 20 °C. The encircled areas and arrows indicate the sequence of precipitation and dissolution for a single Au NP under equilibrium conditions.

Knowing the equilibrium conditions from the previous experiment, we started to verify the proposed radiolysis model of radical-induced redox chemistry in the LCTEM by varying the electron dose rate at ambient temperature. The results of the experiment are shown in Figure . The experimental dose rate was set to 10^8 Gy/s, just below the expected dose rate of the Au NPs' precipitation, as determined in the previous experiment. Accordingly, at the dose rate of 10^8 Gy/s, no NPs were formed. After 12 s, the dose rate was increased from 10^8 Gy/s to 10^{12} Gy/s for a period of 15 s, which initiated the precipitation of Au NPs, reaching their average size of 60 nm. After this period, the dose rate was rapidly reduced back to the initial 10^8 Gy/s. At that point, the Au NPs start to shrink, and in less than 10 s the NPs were completely dissolved. The experiment was repeated at the same observation area 100 s later to verify, whether the phenomenon was reproducible. In this new experiment, the area was exposed with a dose rate of 10^{12} Gy/s for 5 s, instead of 15 s, as in the previous experiment. A shorter exposure time resulted in the formation of NPs with an average size of 20 nm. When the dose rate was decreased for the second time to 10^8 Gy/s, NPs were again dissolved in approximately 10 s. A quantitative evaluation of the whole experiment is presented in Figure . It shows the variations of the Au NPs' size as a function of the electron dose rate at room temperature. The black line in the image represents the selected dose rate, while the circles symbolize the measured average size of the NPs. These results confirmed that the electron dose-dependent LCTEM experiments are highly reversible and correlate with the predictions obtained from the TDR diagrams, where the Au NPs' precipitation or dissolution at ambient temperature is positively correlated with the variations of the Au redox concentration ratio, i.e., $[Au(0)]/[Au^+]$ as a function of the electron dose rate. Similar precipitation/dissolution trends were also observed in previous studies by Schneider et al. (Schneider, Norton, Mendel, Grogan, Ross, et al. 2014) and Ahn et al. (Ahn et al. 2015).
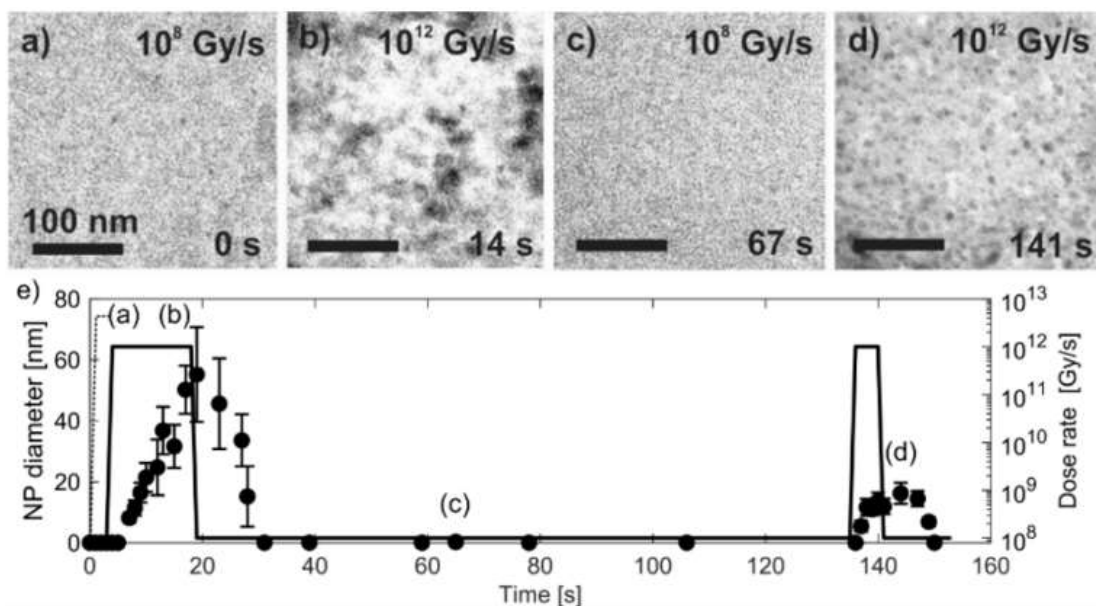
Figure 9: Time-sequenced TEM micrographs acquired from the same specimen area at 25 °C and different electron dose rates (a) 10^8 Gy/s, (b) 10^{12} Gy/s, (c) 10^8 Gy/s, (d) 10^{12} Gy/s (e). Corresponding graphical representation of the Au NPs precipitation and dissolution. The average NPs diameters at every indicated time slot were determined from 10 NPs.

In the next set of the experiments, the electron dose rate was fixed at $6*10^8$ Gy/s, at an initial temperature of 20 °C, just below the experimentally determined boundary conditions for the Au NPs' precipitation. The temperature-dependent experiment started at 25 °C, where the same specimen area was observed for 300 s (Figure), which is a several orders of magnitude longer time than needed to reach the equilibrium concentration of the radiolysis species (Schneider, Norton, Mendel, Grogan, Frances, et al. 2014). This experiment demonstrates that the Au-based aqueous solution is stable at electron dose rates of around 10^8 Gy/s and 20 °C. After a relatively long exposure to the observed specimen area, the temperature was initially increased to 30 °C for a period of 81 s. These conditions did not yield any Au NPs precipitation, which is in accordance with the relatively broad $[Au^{(0)}]/[Au^+]$ gradient field in the temperature domain, as indicated in the TDR diagrams at elevated pressures. When the temperature was increased to 40 °C (t=556s) the Au NPs started to form with an average diameter of around 20 nm (Figure b). When the temperature was decreased back to 25 °C, these precipitated Au NPs were completely dissolved (t=734 s) (Figure c). The reversibility of the phenomenon was again checked by the repeated temperature variations. First, the temperature was raised again to 40°C (t=923s), which resulted in the precipitation of Au NPs with an average diameter of around 20 nm (Figure d). After that, the temperature was lowered back to 25 °C (t=1146s) and the previously precipitated Au NPs were again completely dissolved (Figure e), thus confirming the temperature-dependent reversibility of the Au precipitation-dissolution mechanism.
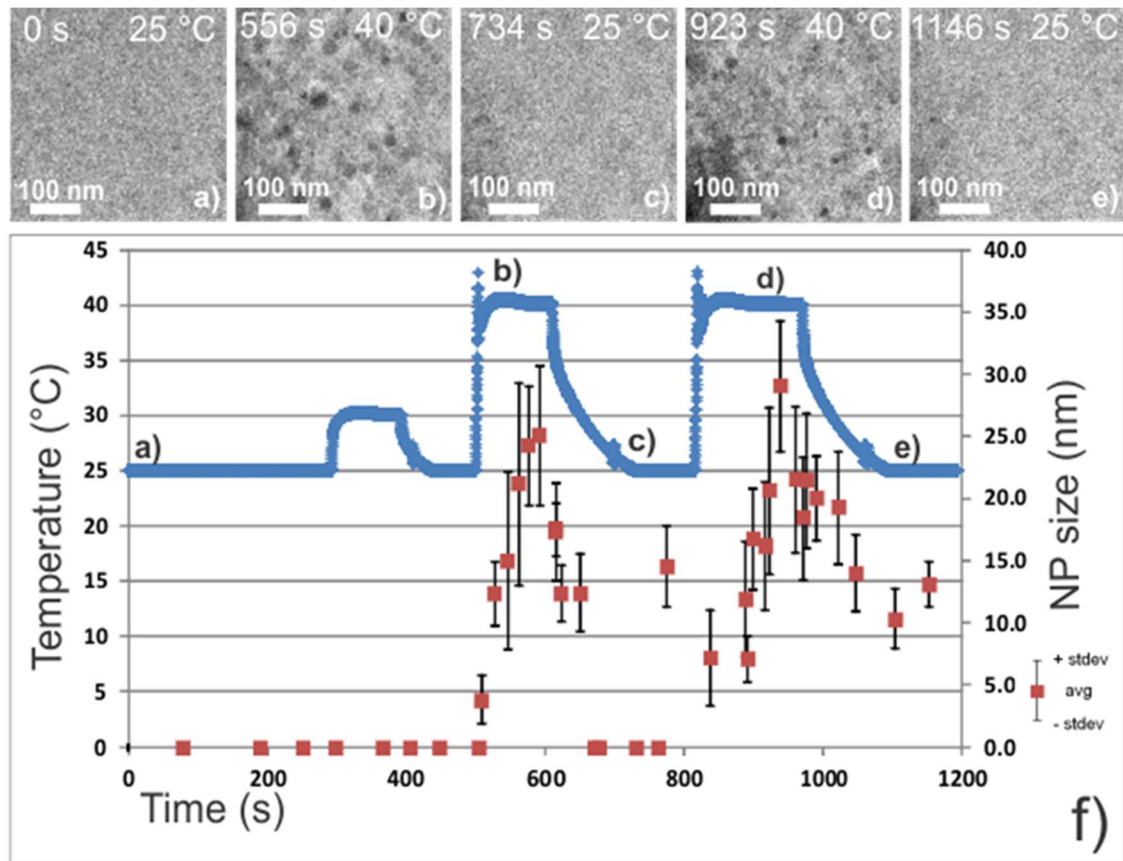
Figure 10: TEM micrographs of the precipitation/dissolution trends of Au NPs as a function of temperature variations between 25 °C and 40 °C on a progressive time scale. Time-sequenced TEM micrographs acquired from the same specimen area at a fixed electron dose rate of $6*10^8$ Gy/s and different temperatures of (a) 25°C, t=0, (b) 40°C, t=556s, (c) 25°C, t=734s, (d) 40°C, t=923s and (e) 25°C, t=1146s (f). The temperature-time profile is indicated by the blue line. The average NPs diameters at every indicated time slot were determined from 10 NPs.

These observations contradict the basic understanding of precipitation/dissolution trends that would typically be observed in comparable ex-situ tabletop experiments, if we neglect the radiolysis-induced redox chemistry. Namely, it is well accepted that the precipitation of Au NPs from an Au aqueous solution at low pH values is typically provoked by the elevated temperature (Schneider, Norton, Mendel, Grogan, Ross, et al. 2014).

However, this process is not reversible and cannot lead to Au NPs' dissolution during a temperature drop in the system. Consequently, this phenomenon can only be explained by the fact that temperature changes provoke significant variations in the equilibrium concentration of the radiolysis species, yielding substantial changes to the Au redox concentration ratios, finally resulting in the reversible precipitation/dissolution of Au NPs. These experimental results are therefore consistent with the [Au(0)]/[Au$^+$] trends indicated in the TDR diagrams for elevated pressure values.

The ex-situ SAED and EDS analyses confirmed that the observed NPs belong to face-centered cubic gold (Figure).
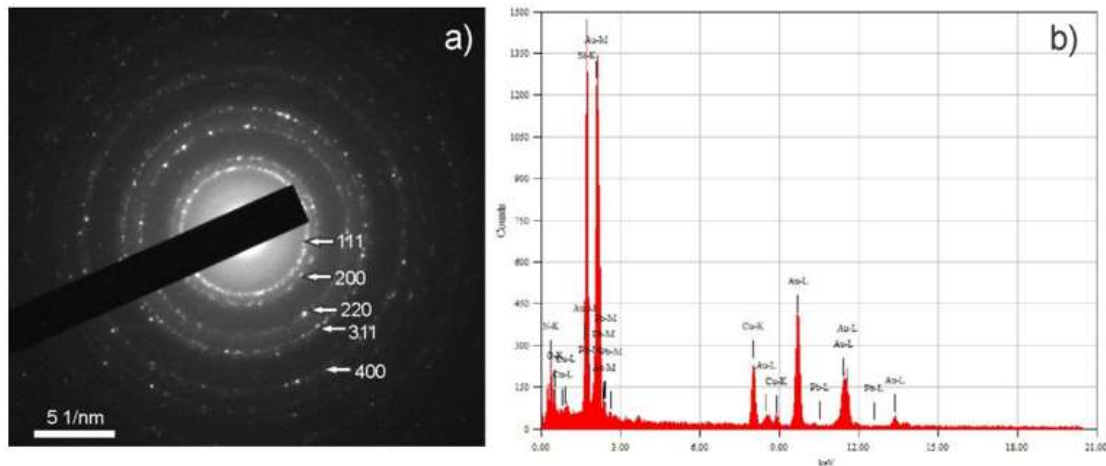
Figure 11: TEM analysis of Au NPs of air-dried samples. a) SAED analysis shows they are FCC Au (ICSD = 52249), b) which was additionally confirmed with an EDS analysis.

Conclusions

As shown, radiolysis effects are an undesirable consequence of the LCTEM technique. The proposed solutions to mitigate the effects of electron radiolysis are:

1) The use of radiolysis models as demonstrated, making it possible to show the threshold, at which the observed processes are radiolytically induced and those which are not.
2) Observing the liquid with a "single exposure technique" - only during the imaging.
3) The use of STEM can greatly reduce dose rates, because at any one single time only one small area is electron irradiated (Khelfa et al. 2019).
4) Use of liquids that are less prone to radiolysis (Bell, Rodgers, and Burrows 1977).
5) Use of liquids that are not highly volatile or corrosive since they can evaporate before the liquid cell is sealed.
6) Use of highly diluted solutions/solutions with a low concentration of dissolved ions (e.g., in the mM range), since dissolved ions in a diluted solution, react less with the radiolysis species.
7) Whenever possible, direct flow experiments with high flow rates are suggested, to flush the radiolysis species out of the observation area of the liquid cell.
8) Preparations of liquid samples just before the insertion into the liquid cell to prevent the formation artifacts formed from aging of the solution.
9) Observation of samples at reduced dose rates (decreasing spot size, use of small condenser apertures).
10) Observing samples for an as short time as still feasible.
11) Careful planning of the LCTEM experiments: with the "lowest necessary exposure to ionizing radiation" principle. This means that the sample should be observed only at such a low electron dose and for a such short time, that the image/video/data with only the predetermined required resolution is obtained and not higher than is needed.
12) TEM alignment needs to be performed before the insertion of the LCTEM holder or use of auto-alignment procedures (Koster and de Ruijter 1992), since during the TEM alignment high electron doses are expected.
13) Use of ultra-thin graphene liquid cells (instead of SiN) that allows smaller electron dose rates for the same brightness/contrast of the image.
14) Use of liquid cells, where the ratio between the windows and the entire volume of the liquid cells is very large, so that diffusion of the radiolysis species is prolonged.
15) Thorough cleaning after each use of all the components of the liquid cell (chips, holder, lids, necessary tools, internal and external tubing) with alcohol, deionized water, and plasma so that contaminants from previous experiments are completely removed, preventing those remaining particles from acting as nuclei for a heterogeneous nucleation process. Frequent replacements of expendable parts (e.g., internal tubing) are suggested.
16) Avoiding the reuse of chips that have already been used in previous experiments.

17) Use of a dust-free clean-room environment for preparing samples and the assembly of the liquid cell to prevent contaminants entering to the solution. Also, the sample preparation room should have temperature/humidity control.

This report is based on a PhD thesis of Bojan Ambrožič entitled "In situ synthesis and growth of nanoparticles using a liquid cell transmission electron microscopy technique".

Some sections are partially based on an article by Ambrožič et al., (Ambrožič et al. 2019) and presents an overview of the calculation for the kinetic radical-induced redox model.

References

Ahmad, Nabeel, Yann Le Bouar, Christian Ricolleau, and Damien Alloyeau. 2017. "Growth of Dendritic Nanostructures by Liquid-Cell Transmission Electron Microscopy: A Reflection of the Electron-Irradiation History." *Advanced Structural and Chemical Imaging* 2 (1): 9. https://doi.org/10.1186/s40679-016-0023-0.

Ahn, Tae-Young, Seung-Pyo Hong, Seong-Il Kim, and Young-Woon Kim. 2015. "In Situ Liquid-Cell Transmission Electron Microscopy for Direct Observation of Concentration-Dependent Growth and Dissolution of Silver Nanoparticles." *RSC Adv.* 5 (100): 82342–45. https://doi.org/10.1039/C5RA14879K.

Alloyeau, Damien, Walid Dachraoui, Yasir Javed, Hannen Belkahla, Guillaume Wang, Hélène Lecoq, Souad Ammar, et al. 2015. "Unravelling Kinetic and Thermodynamic Effects on the Growth of Gold Nanoplates by Liquid Transmission Electron Microscopy." *Nano Letters* 15 (4): 2574–81. https://doi.org/10.1021/acs.nanolett.5b00140.

Ambrožič, Bojan, Anže Prašnikar, Nejc Hodnik, Nina Kostevšek, Blaž Likozar, Kristina Žužek Rožman, and Sašo Šturm. 2019. "Controlling the Radical-Induced Redox Chemistry inside a Liquid-Cell TEM." *Chemical Science* 10 (38): 8735–43. https://doi.org/10.1039/c9sc02227a.

Anderson, Robert F, Borivoj Vojnovic, and Barry D Michael. 1985. "The Radiation-Chemical Yields of H_3O^+ and OH^- as Determined by Nanosecond Conductimetric Measurements." *Radiation Physics and Chemistry* 26 (3): 301–3. https://doi.org/10.1016/0146-5724(85)90068-8.

Armstrong, D. A., Huie; R. E.; Lymar, S.;Koppenol, W. H.;Merényi, G.; Neta, P.; Ruscic, B.; Stanbury, D. M.; Steenken, S. 2015. "Standard Electrode Potentials Involving Radicals in Aqueous Solution : Inorganic Radicals (IUPAC Technical Report)." *Pure and Applied Chemistry* 87: 1139–1150.

Atinault, E., V. De Waele, U. Schmidhammer, M. Fattahi, and M. Mostafavi. 2008. "Scavenging of Es^- and $OH^.$ Radicals in Concentrated HCl and NaCl Aqueous Solutions." *Chemical Physics Letters* 460 (4–6): 461–65. https://doi.org/10.1016/j.cplett.2008.06.048.

Battino, R. 1981a. "Solubility Data Series, Volume 7, Oxygen and Ozone." In *IUPAC-NIST Solubility Database, Version 1.1*. https://doi.org/10.18434/T4QC79.

———. 1981b. "Volume 7, Oxygen and Ozone." In *IUPAC-NIST Solubility Database*, 1–5. Oxford, U.K.: Pergamon Press. https://doi.org/10.18434/T4QC79.

Bell, Ian P., Michael A.J. Rodgers, and Hugh D. Burrows. 1977. "Kinetic and Thermodynamic Character of Reducing Species Produced on Pulse Radiolysis of Acetonitrile." *Journal of the Chemical Society, Faraday Transactions 1: Physical Chemistry in Condensed Phases* 73: 315–26. https://doi.org/10.1039/F19777300315.

Bratsch, G. Stephen. 1989. "Standards Electrode Potentials and Temperature Coefficients in Water at 298.15 K." *J. Phys. Chem. Ref. Data* 18 (1): 1– 21.

Buxton, George V, Clive L Greenstock, W Phillips Helman, and Alberta B Ross. 1988. "Critical Review of Rate Constants for Reactions of Hydrated Electrons, Hydrogen Atoms and Hydroxyl Radicals in Aqueous Solution." *Journal of Physical and Chemical Reference Data* 17 (2): 513.

https://doi.org/10.1063/1.555805.

Egerton, R. F., P. Li, and M. Malac. 2004. "Radiation Damage in the TEM and SEM." *Micron* 35 (6): 399–409. https://doi.org/10.1016/j.micron.2004.02.003.

Elliot, A.J. Bartels, D.M. 2009. "The Reaction Set, Rate Constants and g-Values for the Simulation of the Radiolysis of Light Water over the Range 20° to 350°C Based on Information Available in 2008; Report AECL No. 153-127160-450-001; Atomic Energy of Canada Ltd.: Chalk River, ON, 2009."

Ershov, B.G., E.V. Abkhalimov, R.D. Solovov, and V.I. Roldughin. 2016. "Gold Nanoparticles in Aqueous Solutions: Influence of Size and PH on Hydrogen Dissociative Adsorption and Au(III) Ion Reduction." *Physical Chemistry Chemical Physics* 18 (19). https://doi.org/10.1039/c6cp01996j.

Ghosh Mazumdar, A. S. and Hart, Edwin J. 1968. "A Pulse Radiolysis Study of Bivalent and Zerovalent Gold in Aqueous Solutions." In *Radiation Chemistry*, 193–209. https://doi.org/10.1021/ba-1968-0081.ch013.

Green, N. J.B., M. J. Pilling, S. M. Pimblott, and P. Clifford. 1990. "Stochastic Modeling of Fast Kinetics in a Radiation Track." *Journal of Physical Chemistry* 94 (1): 251–58. https://doi.org/10.1021/j100364a041.

Grogan, J M, N M Schneider, F M Ross, and H H Bau. 2014. "Bubble and Pattern Formation in Liquid Induced by an Electron Beam." *Nano Lett* 14: 0–5. https://doi.org/10.1021/nl404169a.

Grogan, Joseph M, Nicholas M N.M. Schneider, Frances M. Ross, and Haim H Bau. 2014. "Bubble and Pattern Formation in Liquid Induced by an Electron Beam." *Nano Lett* 14 (1): 0–5. https://doi.org/10.1021/nl404169a.

Habahchi, F. 1967. *Kinetics and Mechanism of Gold and Silver Dissolution in Cyanide Solution*. Montana Bureau of Mines Geological Bulletin 59.

Hayon, E. 1963. "Radiolysis of Air-Free Aqueous Solutions of Hydrogen Peroxide." *Service de Chimie-Physique C.E.N. Saclay*, 1059–67.

Hill, M. A., and F. A. Smith. 1994. "Calculation of Initial and Primary Yields in the Radiolysis of Water." *Radiation Physics and Chemistry* 43 (3): 265–80. https://doi.org/10.1016/0969-806X(94)90190-2.

Hochanadel, C. J. 1952. "Effects of Cobalt γ-Radiation on Water and Aqueous Solutions." *The Journal of Physical Chemistry* 56 (5): 587–94. https://doi.org/10.1021/j150497a008.

Khelfa, Abdelali, Caroline Byun, Jaysen Nelayah, Guillaume Wang, Christian Ricolleau, and Damien Alloyeau. 2019. "Structural Analysis of Single Nanoparticles in Liquid by Low-Dose STEM Nanodiffraction." *Micron* 116 (September 2018): 30–35. https://doi.org/10.1016/j.micron.2018.09.008.

Koster, A. J., and W. J. de Ruijter. 1992. "Practical Autoalignment of Transmission Electron Microscopes." *Ultramicroscopy* 40 (2): 89–107. https://doi.org/10.1016/0304-3991(92)90052-L.

Lingane, James J. 1962. "Standard Potentials of Half-Reactions Involving + 1 and + 3 Gold in Chloride Medium: Equilibrium Constant of the Reaction AuCl4− + 2Au + 2Cl− = 3AuCl2−." *Journal of Electroanalytical Chemistry (1959)* 4 (6): 332–42. https://doi.org/10.1016/0022-0728(62)80079-5.

Ngo, Thao, and Hong Yang. 2015. "Toward Ending the Guessing Game: Study of the Formation of Nanostructures Using in Situ Liquid Transmission Electron Microscopy." *Journal of Physical Chemistry Letters* 6 (24): 5051–61. https://doi.org/10.1021/acs.jpclett.5b02210.

Nielsen, Michael H., Dongsheng Li, Hengzhong Zhang, Shaul Aloni, T. Yong-Jin Han, Cathrine Frandsen, Jong Seto, Jillian F. Banfield, Helmut Cölfen, and James J. De Yoreo. 2014. "Investigating Processes of Nanocrystal Formation and Transformation via Liquid Cell TEM." *Microscopy and Microanalysis* 20 (02): 425–36. https://doi.org/10.1017/S1431927614000294.

Pacławski, K. and Fitzner, K. 2006. "Kinetics of Reduction of Gold(III) Complexes Using H_2O_2." *Metallurgical and Materials Transactions B* 37B (5): 703–14. https://doi.org/10.1007/s11663-006-0054-3.

Pastina, Barbara, and Jay A Laverne. 2001. "Pastina_2001_Effect of Molecular Hydrogen on Hydrogen Peroxide in Water Radiolysis.Pdf," 9316–22.

Prototochips Inc. n.d. "Poseidon Select: TEM Micrscopy Liquid Cell."
https://www.protochips.com/products/poseidon-select/.

R Winston Revie; Herbert Henry Uhlig. 2011. *Uhlig's Corrosion Handbook*. Electroche. Wiley.

Schneider, Nicholas M., Michael M. Norton, Brian J. Mendel, Joseph M. Grogan, Frances M. Ross, and Haim H.
Bau. 2014. "Electron-Water Interactions and Implications for Liquid Cell Electron Microscopy." *Journal of Physical Chemistry C* 118 (38): 22373–82. https://doi.org/10.1021/jp507400n.

Schneider, Nicholas M, Michael M Norton, Brian J Mendel, Joseph M Grogan, M Frances, and Haim H Bau.
2014. "Electron - Water Interactions and Implications for Liquid Cell Electron Microscopy – Supporting Information." *The Journal of Physical Chemistry C* 118 (38): 22373–82.

Schwarz, Harold A. 1981. "Free Radicals Generated by Radiolysis of Aqueous Solutions" 58 (2): 101–5.
https://doi.org/10.1021/ed058p101.

Shin, Dongha, Jong Bo Park, Yong Jin Kim, Sang Jin Kim, Jin Hyoun Kang, Bora Lee, Sung Pyo Cho, Byung Hee
Hong, and Konstantin S. Novoselov. 2015. "Growth Dynamics and Gas Transport Mechanism of Nanobubbles in Graphene Liquid Cells." *Nature Communications* 6: 1–6.
https://doi.org/10.1038/ncomms7068.

Wang, S., V. Petzold, V. Tripkovic, J. Kleis, J. G. Howalt, E. Skúlason, E. M. Fernández, et al. 2011. "Universal
Transition State Scaling Relations for (de)Hydrogenation over Transition Metals." *Physical Chemistry Chemical Physics* 13: 20760–65. https://doi.org/10.1039/c1cp20547a.

Williamson, M. J., R. M. Tromp, P. M. Vereecken, R. Hull, and F. M. Ross. 2003. "Dynamic Microscopy of
Nanoscale Cluster Growth at the Solid-Liquid Interface." *Nature Materials* 2 (8): 532–36.
https://doi.org/10.1038/nmat944.

Woehl, Taylor J., Katherine L. Jungjohann, James E. Evans, Ilke Arslan, William D. Ristenpart, and Nigel D.
Browning. 2013. "Experimental Procedures to Mitigate Electron Beam Induced Artifacts during in Situ Fluid Imaging of Nanomaterials." *Ultramicroscopy* 127: 53–63.
https://doi.org/10.1016/j.ultramic.2012.07.018.

Xin, Huolin L, Kaiyang Niu, Daan Hein Alsem, and Haimei Zheng. 2013. "In Situ TEM Study of Catalytic
Nanoparticle Reactions in Atmospheric Pressure Gas Environment." *Microscopy and Microanalysis : The Official Journal of Microscopy Society of America, Microbeam Analysis Society, Microscopical Society of Canada* 19 (6): 1558–68. https://doi.org/10.1017/S1431927613013433.

Yang, Yang, Changqing Dai, Adrian Fisher, and Yanchun Shen. 2017. "A Full Understanding of Oxygen Reduction
Reaction Mechanism on Au (1 1 1) Surface."

Young, C. L. 1981a. "Volume 5/6, Hydrogen and Deuterium." In *IUPAC-NIST Solubility Database*, 1–3. Oxford,
U.K.: Pergamon Press. https://doi.org/10.18434/T4QC79.

Young, C.L. 1981b. "Solubility Data Series, Volume 5/6, Hydrogen and Deuterium." In *IUPAC-NIST Solubility
Database, Version 1.1*. https://doi.org/10.18434/T4QC79.

Zhu, Guomin, Yingying Jiang, Wei Huang, Hui Zhang, Fang Lin, and Chuanhong Jin. 2013. "Atomic Resolution
Liquid-Cell Transmission Electron Microscopy Investigations of the Dynamics of Nanoparticles in Ultrathin Liquids." *Chemical Communications* 49 (93): 10944. https://doi.org/10.1039/c3cc46667a.